RSC Advances

ROYAL SOCIETY OF CHEMISTRY

www.rsc.org/advances

Facile synthesis of pseudo-peanut shaped hematite iron oxide nano-particles and their promising ethanol and formaldehyde sensing characteristics

P. Das[a,b], B. Mondal[a], K. Mukherjee[a]*

[a]Centre for Advanced Materials Processing, CSIR-Central Mechanical Engineering Research Institute, Durgapur-713209, India

[b]CSIR-Central Mechanical Engineering Research Institute-Academy of Scientific and Innovative Research Ph. D Scholar, Durgapur-713209, India

*Corresponding Author, Email: kalisadhanm@yahoo.com; Ph: Tel.: +91-343-6510255 (O); +91-9775552143 (m)

Abstract: Herein, pseudo-peanut shaped hematite iron oxide nano-particles are prepared through a facile cost effective wet chemical synthesis route. The synthesized particles are characterized in terms of their phase formation behavior, morphological features and used for sensing ethanol and formaldehyde vapors. The sensing characteristics (response %, response time, recovery time, selectivity coefficient) are investigated by varying the operating temperature (300-375^{o}C) of the sensor and concentration (20-200 ppm) of the studied vapors. The sensor shows promising response towards ethanol and formaldehyde vapors. In the studied operating temperature range, the response of the sensor towards ethanol is found better than formaldehyde. The cross-selectivity issue of the sensor has been addressed using the variation of selectivity coefficient with the exposure time of the vapors. For sensing ethanol and formaldehyde vapors, the response of the pseudo-peanut shaped particles is compared with poly-disperse type hematite particles. As compared to the poly-disperse particles, peanut like structures are found superior for sensing the studied vapors.

Keywords: Iron oxide; Nano-particle; Auto-combustion; Gas sensor; Ethanol; Formaldehyde

1. Introduction:

Iron oxide has been studied extensively for variety of applications including but not limited to magnetic, drug delivery, catalysis, water splitting, imaging, rechargeable lithium batteries, gas sensors etc [1-7]. The morphological parameters (e.g. size, shape, porous nature etc) of iron oxide particles are often found to play significant role in modulating its surface as well as catalytic properties. The synthesis of iron oxide particles with controlled shape and size has thus attracted considerable academic and technological interest [8-16]. A number of physical/ chemical vapor deposition techniques and a series of wet chemical methods (including co-precipitation, sol-gel, hydrothermal process etc) have been used for the synthesis iron oxide particles. Among these methods, wet chemical procedures are considered advantageous due to their simplicity and low processing cost. However, the synthesis of phase pure iron oxide remains challenging due to the existence of its various possible composition (e.g. goethite (α-FeOOH), akaganeite (β-FeOOH), lepidocrocite (γ-FeOOH), feroxyhyte (δ-FeOOH), wustite (FeO), hematite (α-Fe_2O_3), maghemite (γ-Fe_2O_3) etc) [17-19]. Under ambient conditions, hematite (α-Fe_2O_3) is considered as the most stable form of iron oxide [19-20]. Hematite iron oxide has attracted considerable attention for variety of emerging applications due to its low cost, high resistance to corrosion and environmental safety [7, 21-23]. To meet the increasing technological demand, the cost effective synthesis of well ordered hematite phase iron oxide nano-particles is important. In the present work, pseudo-peanut shaped hematite nano-particles are synthesized through template free glycine mediated facile self combustion route. The phase formation behavior and the microstructure evolution of the synthesized particles are characterized using X-ray diffraction and electron microscope image analyses respectively. Additionally, the synthesized particles are studied in terms of their ethanol and formaldehyde

sensing characteristics (e.g. response %, response recovery time, selectivity coefficient etc). Volatile ethanol and formaldehyde cause severe harmful effect on environment due to their toxic nature. Breathing of ethanol and formaldehyde vapor can affect the immune system of human health. Acute exposure of these organic vapors again may irritate the eyes, nose, throat, and thus expedite the formation of cough and wheeze. Asthma-like respiratory problems and skin irritation are also common by the long term exposure of formaldehyde [24-25]. The sensitive detection of these organic pollutants using low cost sensors seems to be highly demanding. It has been found that the pseudo-peanut shaped hematite iron oxide particles are promising for the detection of low concentration (~ 20 ppm) of ethanol and formaldehyde. For the detection of ethanol and formaldehyde vapors, the response of hematite phase peanut shaped particles are further compared with the poly-disperse particles. It is found that as compared to poly-disperse particles, peanut shaped particles are more sensitive towards the studied vapors. An attempt is made to understand the underlying reason for higher response of the peanut shaped particles than the poly-disperse particles. The facile synthesis of peanut shaped hematite iron oxide nano-particles using cost effective wet chemical route and the subsequent investigation on their ethanol and formaldehyde sensing characteristics are not reported yet in open literature. The present study is therefore significant for iron oxide as well as gas sensor related research activities.

2. Experimental:

Pseudo-peanut shaped hematite iron oxide nano-particles are prepared from iron (III) nitrate through wet chemical based self-combustion route. The schematic flow diagram for the synthesis of peanut shaped iron oxide nano-particles is shown in Figure 1. For synthesis, iron (III) nitrate is first dissolved in distilled water followed by the addition of three mole equivalent of solid

glycine. Glycine (consists of one $–NH_2$ and one –COOH group), a simple amino acid is used here as fuel for combustion process and. It also makes complex with metal precursor [26-29]. The strong interaction of iron (III) with glycine is confirmed by the immediate color change when these are mixed together. For the evaporation of the liquid content and to produce a concentrated mass, the prepared solution is heated for one hour at 100°C. The concentrated mass is then heated at 150°C until the auto combustion is initiated through fuming, smoldering and frothing processes. The auto combustion is considered as a thermally induced redox reaction where the glycine and nitrate ion (NO_3^-) play the role of reducing and oxidizing agent respectively. Such auto-combustion process produces an enormous heat which initiates the decomposition of iron (III)-glycine complex followed by the formation of dried iron oxide particles [30].

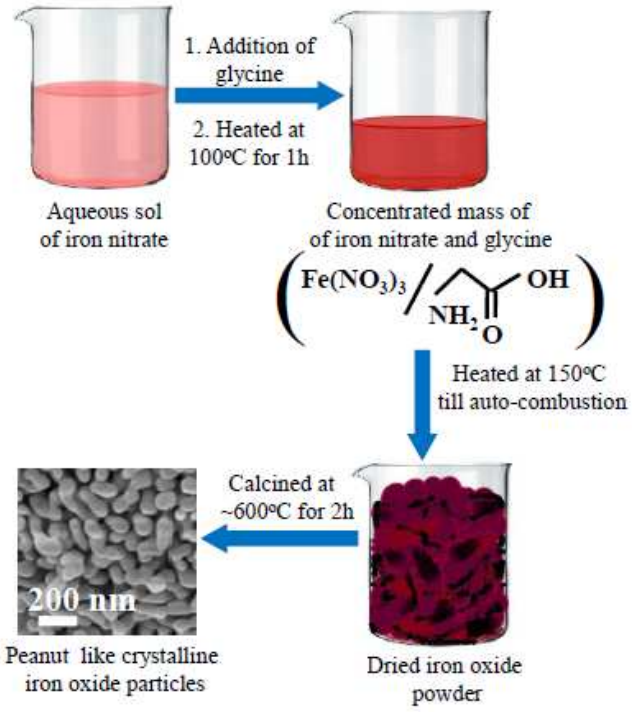

Figure 1. Flow diagram for the synthesis of peanut like hematite iron oxide particles

Since the process is completed within a very short period, the nucleations of the particles also get restricted resulting peanut like structures. The dried particles are calcined further at 600^{o}C for 2 hours to obtain well crystalline hematite iron oxide powder.

The phase formation behavior of the synthesized iron oxide particles is studied by analyzing the X-ray diffraction (XRD) pattern. For the synthesized iron oxide particles, the formation of iron-oxygen (Fe-O) bond is confirmed in Fourier transform infra-red (FTIR) spectra. The surface morphology of the crystallized particles is characterized using scanning electron microscope (SEM) and transmission electron microscope (TEM).

For preparing the sensing element, the calcined particles are pressed in the form of circular disc (12 mm diameter, 2 mm thickness). To measure its electrical characteristics, silver paste based strip electrodes are prepared on one surface of the sensing element. The ethanol and formaldehyde sensing characteristics of the sensing element is measured using a static flow gas sensing measurement set-up developed in the laboratory. The details of the set-up have already been described elsewhere [31]. The sensing characteristics are measured by varying the operating temperature (300-375^{o}C) of the sensor and concentration (20-200 ppm) of ethanol and formaldehyde. Before performing the sensing experiments, the sensor is kept at the respective operating temperature for ~30 min to achieve a constant resistance in air (R_{air}). During the sensing measurements, the surface current of the sensor is measured by applying a fixed voltage on one of the electrode. From the measured value of the equilibrated resistance of the sensor in air (R_{air}) and in vapor (R_{vap}), the response % (S) of the sensor is estimated using the following relation [31].

$$S = \frac{\left(R_{air} - R_{vap}\right) \times 100}{R_{air}} \qquad (1)$$

The time taken by the sensing element for changing 63% of its resistance under the exposure of vapor and air is defined as response and recovery times respectively.

3. Results and discussions

3.1. Phase and micro-structural characteristics of the synthesized iron oxide

Figure 2 shows the X-ray diffraction (XRD) pattern (under CoK_{α} radiation) of pseudo-peanut shaped iron oxide particles calcined at 600°C for 2h. The XRD pattern matches well with the standard powder XRD pattern (JCPDS-card-33-0664) of hematite iron oxide.

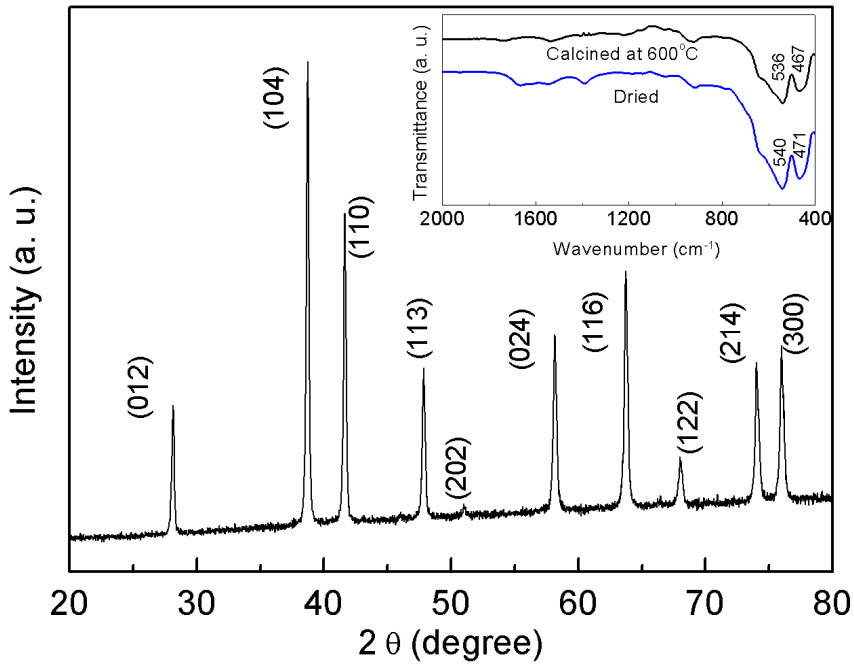

Figure 2. X-ray diffraction pattern of the synthesized iron oxide particles. Inset shows the FTIR spectra of dried and calcined iron oxide particles

The average crystallite size (α) of the particles is estimated using the well known Debye-Scherrer formula as follows.

$$a = \frac{0.89\lambda}{\beta \cos\theta} \qquad (2)$$

where λ is the wavelength of the X-ray used, β is the full width at half maxima (FWHM) of the concerned peaks and θ is the incident grazing angle [32]. Two most prominent peaks [(104) and (110)] are considered for the estimation of average crystallite size. The average crystallite size is estimated to be ~39 nm. The FTIR spectra of dried and calcined iron oxide particles are shown in the inset of Figure 2. The formation of iron oxygen bond (Fe-O) has been observed in both the samples. For the dried particles the Fe-O bonds arise at 540 and 471 cm^{-1}. However, for calcined powders the Fe-O peaks are shifted to 536 and 467^{-1}. For dried and high temperature calcined powders, such shift of Fe-O bonds are reported due to the conversion of iron oxide from maghemite to hematite phase [33]. It is also envisaged from the figure that little organic residues (corresponding the marked C=O, and C-O bonds of glycine) are present in dried particles; whereas these organics are removed mostly when calcined at high temperature (600^{o}C).

The FESEM images of the calcined iron oxide particles are shown in Figure 3 (a). As revealed in the figure, the iron oxide particles resemble the morphology of pseudo-peanut.

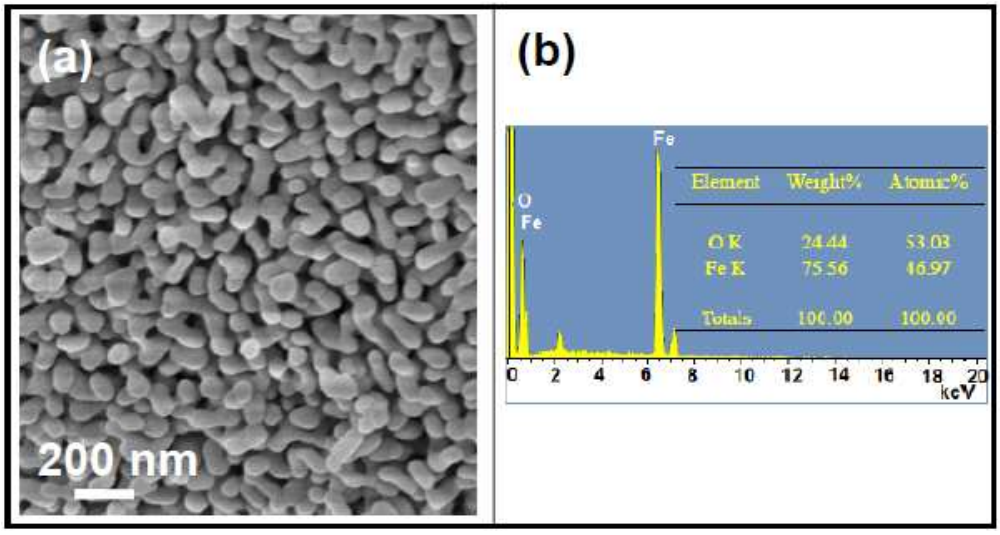

Figure 3. (a) FESEM images of synthesized pseudo-peanut like iron oxide particles (b) EDX spectrum of the synthesized iron oxide.

Precisely, the particles are found to nucleate and grow in one direction. The growth of the particles is not controlled consistently which eventually form shorter as well as longer peanut like structure. The composition of the particles is confirmed by the energy dispersive X-ray spectrum (EDS) (Figure 3 (b)) acquired during the FESEM imaging.

Figure 4 (a) shows the TEM image of the synthesized iron oxide particles. Due to the agglomeration of the particles, the individual peanut like structures is not prominent in the figures. However the directional growth of the particles can be visualized. The high resolution TEM (HRTEM) image recorded on the boundary face of a particle shows the lattice fringes with an inter-planar spacing of about 0.272 nm, which corresponds to the (104) plane of α-Fe_2O_3 (Figure 4 (b)).

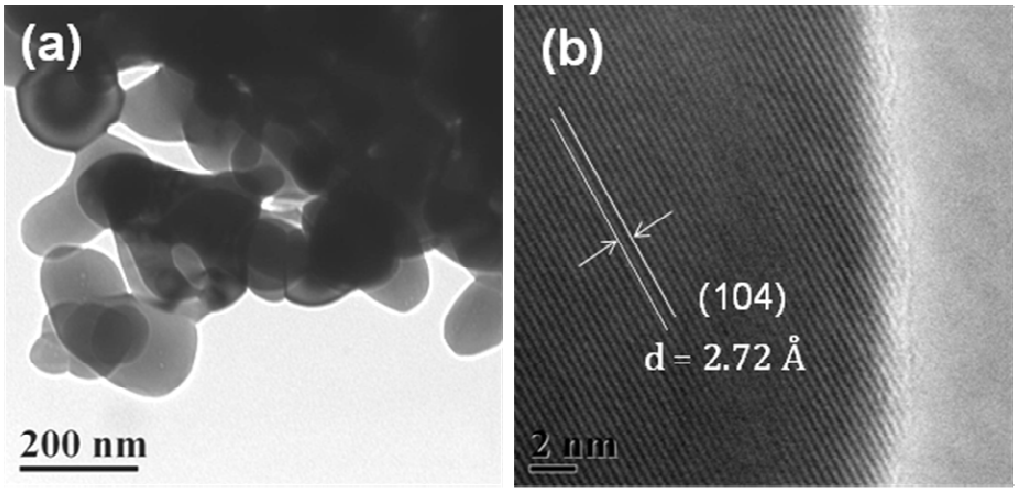

Figure 4. (a) TEM images of synthesized iron oxide particles. (b) HRTEM image shows the lattice fringe of iron oxide particle.

3.2. Ethanol and formaldehyde sensing characteristics of iron oxide sensing elements

The prepared iron oxide based sensing element shows n-type sensing behavior i.e. resistance of the sensor decreases in presence of reducing vapors (e.g. ethanol, formaldehyde). Herein, an

attempt has been made to understand the mechanism for sensing reducing vapors on pseudo-peanut shaped iron oxide particles using Figure 5.

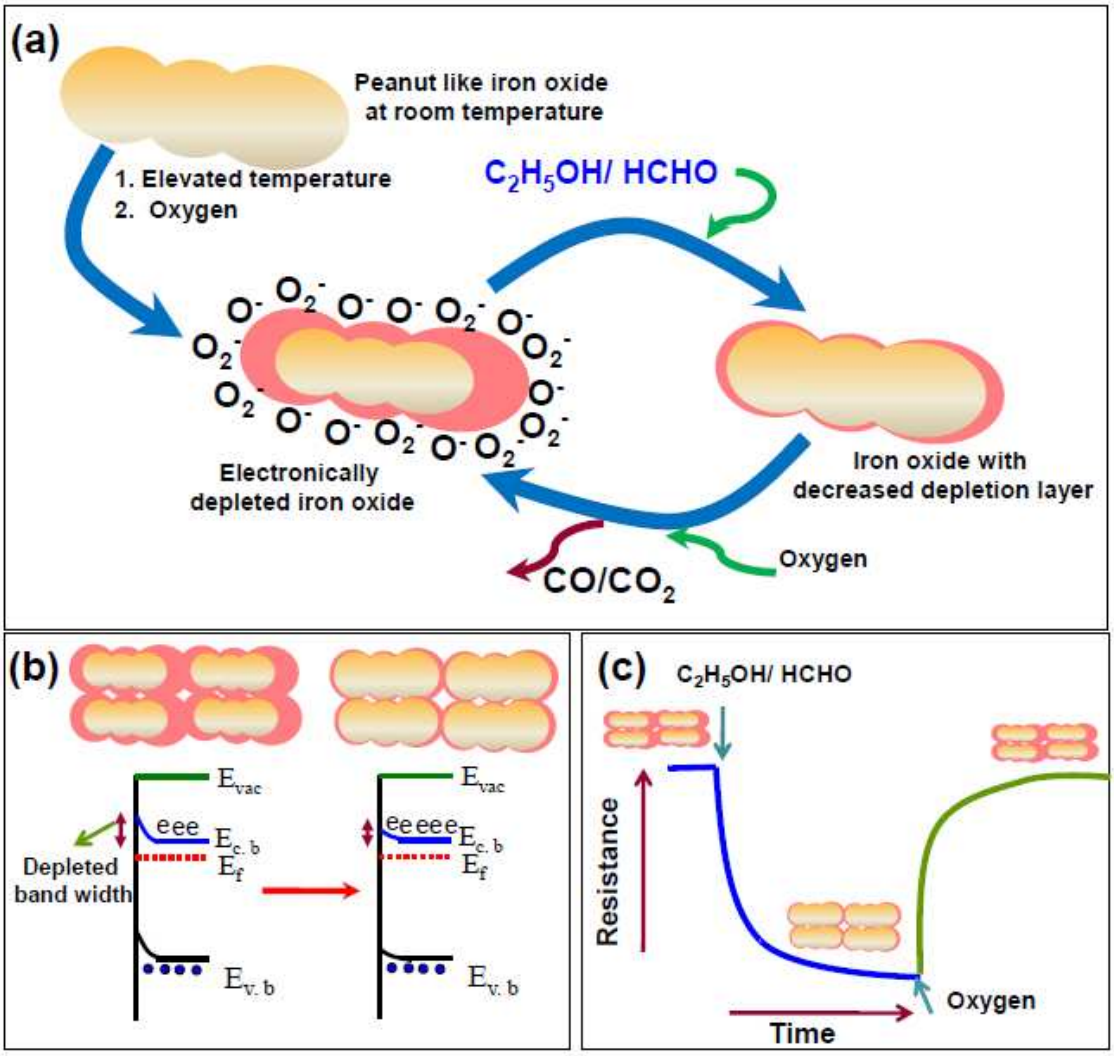

Figure 5. (a) Schematic description for chemi-adsorption of oxygen and the reaction of reducing vapors with chemi-adsorbed oxygen on peanut like iron oxide particles. The respective change in electron depleted layer width is also shown (b) Schematic change in band diagram of iron oxide due to the alteration of electron depleted layer width (c) Correlation of electron depleted layer with the resistance transient obtained during sensing of ethanol and formaldehyde over chemi-resistive iron oxide sensor

In the process of sensing, first oxygen is chemi-adsorbed on the sensor surface (Eqn. (3)-(4)).

$$O_2 + e \rightarrow O_2^- \quad (3)$$

$$O_2 + 2e \rightarrow 2O^- \quad (4)$$

Depending on the surface temperature of the sensor, oxygen may be adsorbed either in atomic (O^-) or in molecular (O_2^-) forms [34-35]. Such chemi-adsorption of oxygen forms an electron depleted layer on the sensing surface which eventually forms a Schottky potential barrier for the inter particle / granular conduction of electron. As a result, the resistance of the sensor increases in presence of oxygen. When the sensor is exposed to reducing gases/ vapors (e.g. ethanol, formaldehyde), the chemi-adsorbed oxygen oxidizes these vapors (Eqn. 5-6) [31, 36].

$$C_2H_5OH + 6O^- \rightarrow 3H_2O + 2CO_2 + 6e^- \quad (5)$$

$$HCHO + O_2^- \rightarrow CO_2 + H_2O + e^- \quad (6)$$

Due to the surface temperature of the sensor, the oxidized products ultimately decompose into carbon monoxide and carbon dioxide. The electrons released due to the oxidation of reducing vapors ultimately come back to the conduction band of the semiconductor resulting the lowering of depleted layer width which in turn decreases the resistance of the sensor. When the sensor is further exposed in oxygen, the surface physi-adsorbed carbon monoxide and carbon dioxide begin to fade away and oxygen is chemi-adsorbed simultaneously on the sensor surface recovering the initial resistance (R_{air}) of the sensor. The chemi-adsorption of oxygen followed by the formation of electron depleted layer on the sensor surface and the subsequent reactions of reducing vapors with the chemi-adsorbed oxygen are presented in Figure 5 (a). In Figure 5 (b), the formation of Schottky barrier is shown using band diagram model. The corresponding resistance transient arises when the sensor is switched back and forth between reducing vapors and oxygen is revealed in Figure 5 (c). Such resistance transient obtained during the response of

reducing gases is termed as response transient and the transient arises during the recovery of the sensor is called recovery transient.

For sensing 200 ppm of ethanol and formaldehyde vapors, Figure 6 (a) and (b) shows the typical response and recovery resistance transient of prepared iron oxide sensor. During the measurement of these resistance transients the sensor is kept at 350 and 300^{o}C respectively. The 'on' and 'off' states of ethanol and formaldehyde vapors are marked in the figures. As reflected from the figures the sensing element shows significant change in resistance when exposed to ethanol and formaldehyde vapors. The resistance change of the sensor is also found reversible when the sensor is switched back and forth between the studied vapors and air.

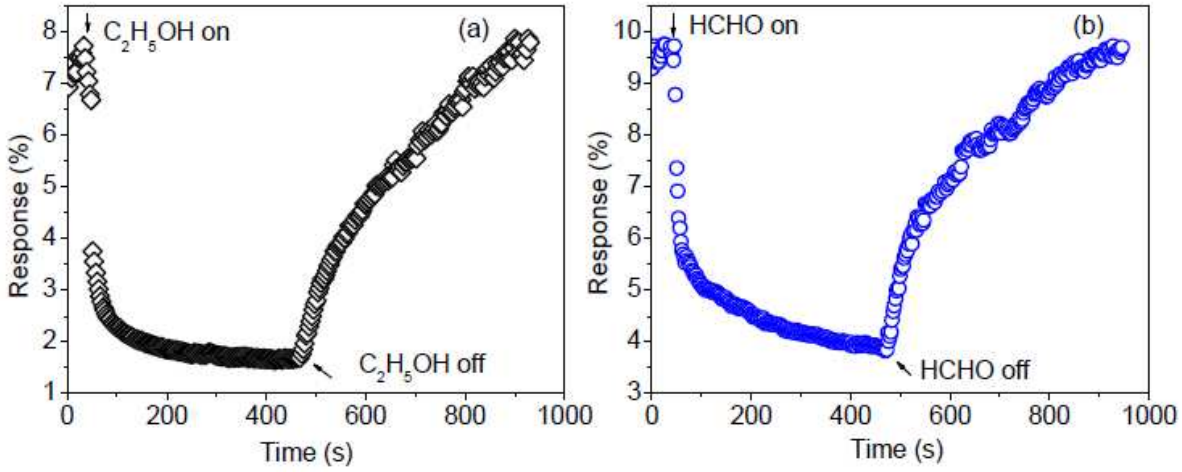

Figure 6. Typical resistance transients obtained during sensing 200 ppm (a) ethanol and (b) formaldehyde over iron oxide based sensing element

For sensing fixed concentration (200 ppm) of ethanol and formaldehyde vapors, the dependence of response % with the sensor operating temperature is shown in Figure 7 (a). As revealed in the figure, the sensor response increases with the sensor operating temperature up to a certain range, attains maxima and decreases afterwards. The underlying reason for such variation of response % with the sensor operating temperature is well established and described

elsewhere [37-38]. The sensor shows maximum response towards ethanol (S~ 78) and formaldehyde (S~ 66) vapors at 350°C. At the studied operating temperature range, the sensor is comparatively less sensitive towards formaldehyde than the ethanol vapor.

The response % of the sensor towards the detection of various concentrations (20-200 ppm) of ethanol and formaldehyde vapors is shown in Figure 7 (b). It is found that the response of the sensor varies linearly with vapor concentration (upto ~100 ppm). However at higher vapor concentration (~200 ppm), the response of the sensor begins to saturate.

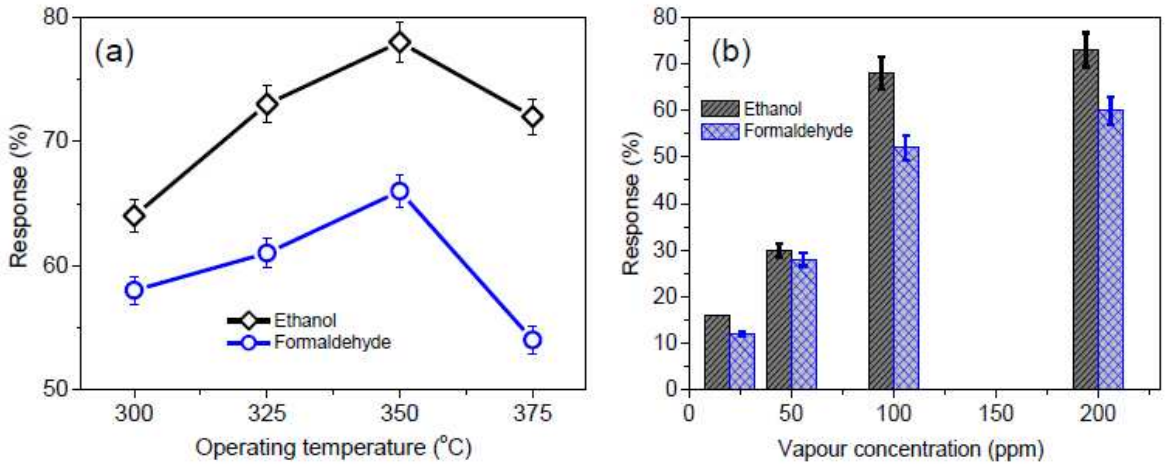

Figure 7. Variation of response % of the sensor with the operating temperature for the detection of 200 ppm ethanol and formaldehyde. (b) Variation of response % of the sensor (kept at ~325°C) with the concentration of vapors.

For the detection of 50-200 ppm ethanol and formaldehyde vapors, the measured resistance transients are shown in Figure 8 (a). From the figure it is clear that in spite of having more response of the sensor towards ethanol, the cross selectivity with formaldehyde cannot be avoided. To address the cross-selectivity of the sensor, here, the term 'selectivity coefficient' is used [39]. At a preset operating temperature, for the detection of fixed concentration of various

gases, the term 'selectivity coefficient' is defined as the ratio of response towards higher sensitive gas to lower sensitive gas.

For detection of ethanol and formaldehyde, here, the selectivity coefficient (κ) of the iron oxide sensor is defined as follows

$$\kappa = S_{EtOH}/S_{HCHO} \quad (7)$$

where the S_{EtOH} and S_{HCHO} are the response % of the sensor towards a fixed concentration of ethanol and formaldehyde at a preset sensor operating temperature.

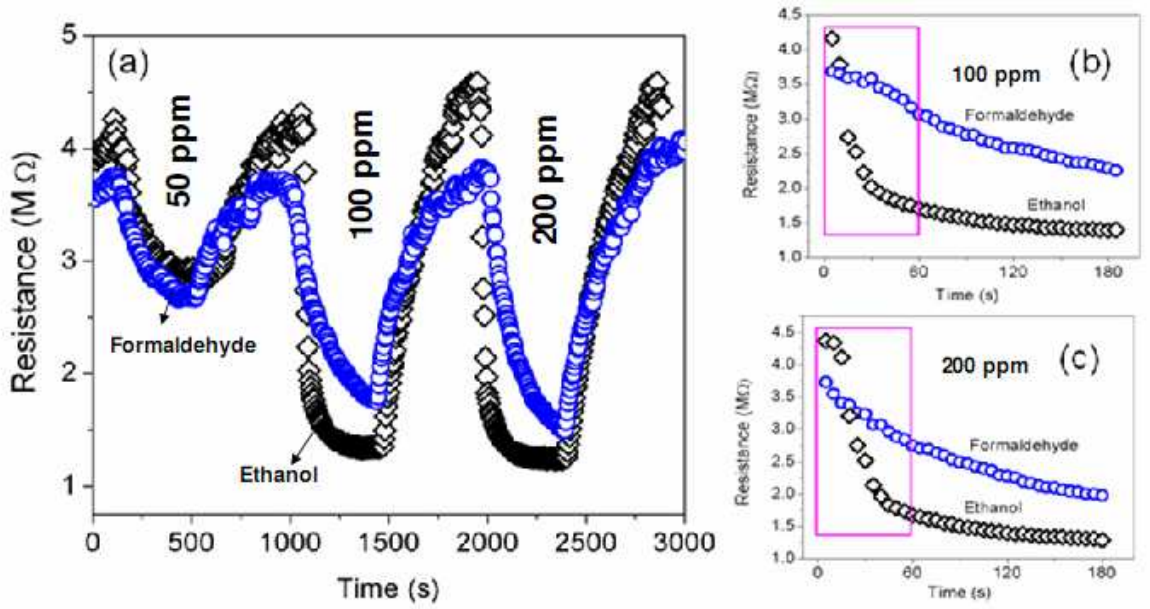

Figure 8. (a) Resistance transient of the iron oxide sensor for the detection of 50-200 ppm of ethanol and formaldehyde at ~325°C. (b) and (c) compare the value of response % towards the detection of 100 and 200 ppm of ethanol and formaldehyde

For the detection of 50-200 ppm ethanol and formaldehyde, the values of selectivity coefficients are estimated by considering the total exposure time as well as exposure for 60 s (summarized in Table 1). As envisaged from the table, the estimated values of κ are low (< 1.3) when the total exposure time is considered. However, one can note that the selectivity coefficient

is pretty high by the immediate (≤ 1 min) exposure of these vapors (Figure 8 (b) and (c)). Therefore, within an exposure limit of 1 min, one can detect the vapors selectively using the peanut shaped iron oxide based sensing element. The development of selective gas/ chemical sensor is a challenging research issue. Various research efforts including the chemical modification of sensing element, kinetic and statistical analyses of the resistance transients are already been reported in the literature [40-42]. However these strategies are still seem to be difficult to address the selectivity issue of the sensors. It is shown here that the variation of selectivity coefficient in different time interval could provide valuable information towards the development of a selective chemical sensor. From Figure 8 (a)-(c), it is also revealed that the response of the sensor towards ethanol is faster than formaldehyde. The estimated response times of the sensor (operating temperature ~325^{o}C) for the detection of 50-200 ppm ethanol and formaldehyde vapors are included in Table 1. It is notable that at a fixed concentration, the response time for the detection of ethanol is faster than formaldehyde detection.

Table 1. Estimated values of response %, response time and selectivity coefficient for iron oxide sensor towards the detection of various concentrations of ethanol and formaldehyde

Parameters	50 ppm		100 ppm		200 ppm	
	EtOH	HCHO	EtOH	HCHO	EtOH	HCHO
Response %	~30	~28	~68	~52	~73	~61
Response time (s)	~150	~200	~50	~180	~45	~160
Selectivity coefficient for the full exposure time	~1.07		~1.27		~1.24	
Selectivity coefficient for 1 min exposure time	~1.18		~6.31		~2.62	

For the detection of ethanol and formaldehyde vapors, the sensing characteristics of hematite phase peanut shaped particles are further compared with the hematite poly-disperse particles. The poly-disperse iron oxide particles are synthesized simply by precipitating aqueous iron-nitrate solution using ammonia. The precipitate is washed with plenty of water to neutralize it (pH ~7) and then dried in oven. The dried particles are calcined in air for 2h to obtain well crystalline hematite iron oxide particles. Fig. 9 (a) shows the FESEM image of the poly-disperse iron oxide particles. As shown in the figure, various size iron oxide particles are closely agglomerated which may result poor diffusion of vapors within the sensing element.

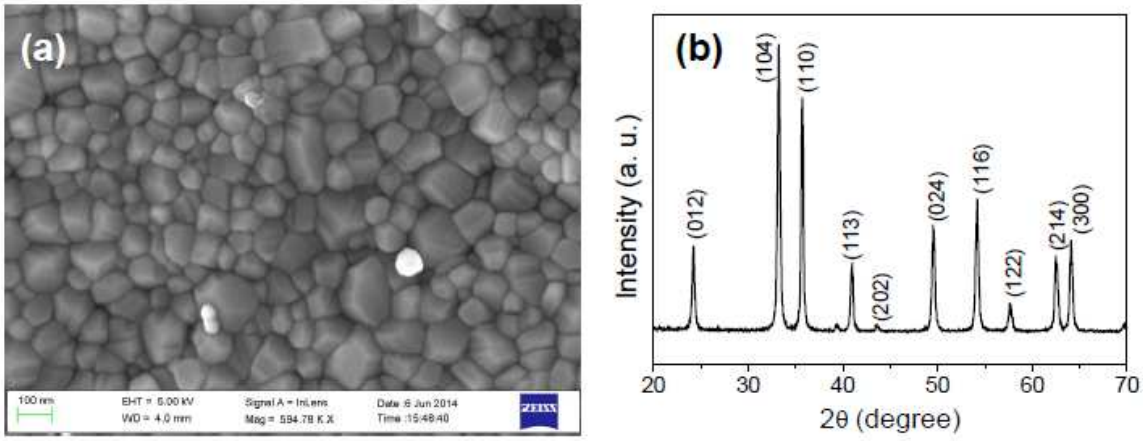

Figure 9. (a) FESEM image (b) X-ray diffraction pattern of poly-disperse hematite iron oxide particles prepared through precipitation route

The hematite phase of the precipitated route derived particles is confirmed in the X-ray diffraction pattern (under CuK_{α} radiation) shown in Figure 9 (b). The resistance transients of poly-disperse particulate measured for sensing 200 ppm ethanol and formaldehyde vapors are shown in Figure 10 (a) and (b) respectively. During the measurement of these resistance transients, the operating temperature of the sensor is kept fixed at ~350^{o}C. For detection of 200

ppm ethanol and formaldehyde vapors, the operating temperature dependent response of the peanut and poly-disperse particle based hematite sensing element is shown in Figure 10 (c).

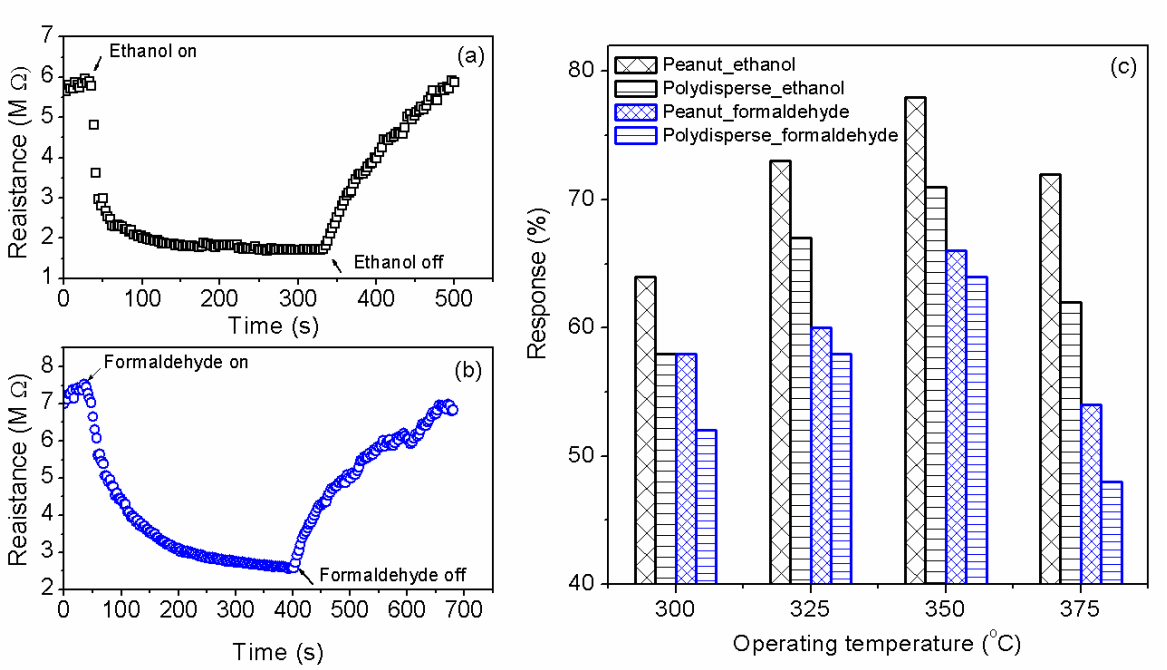

Figure 10. Resistance transients of the poly-disperse particle based sensing element for detection of 200 ppm (a) ethanol and (b) formaldehyde. (c) The operating temperature dependent responses of peanut and poly-disperse particle based sensing element for detection of 200 ppm ethanol and formaldehyde vapors.

As envisaged from Figure 10 (c), within the studied operating temperature range the peanut shaped hematite particles show superior response (towards both ethanol and formaldehyde) than poly-disperse hematite particles. The underlying reason that improves the response of the peanut shaped particles is not clearly understood. However, the size and shape of the peanut like particles are supposed to be more appropriate for achieving superior chemi-resistive type response towards reducing vapors. By virtue of the shape, the peanut like particles produces adequate porous regions which may enhance the diffusion of vapors through the sensing element (ref: Figure 3 (a)). On contrary, poly-disperse particles are expected to produce less porosity

when compacted in the form of sensing element (ref: Figure 9 (a)). The diffusion of vapors through the poly-disperse particulate sensing element eventually gets hindrance leading to lower response of the sensor. In addition, the nearly one dimensional growth of peanut like particles assist them to be depleted (by the chemi-adsorbed oxygen) more than the poly-disperse (having the larger particles as well) particles which may improve the response of the pseudo-peanut shaped particles.

4. Conclusion

Ethanol and formaldehyde are common as solvent in variety of industrial sectors. These organics are volatile in nature and affect the environment immensely. Acute exposure of these organic vapors may irritate the eyes, nose, throat and create asthama like respiratory problems for humans. The detection of such organic pollutants using low cost sensors is thus very demanding. In the present work, promising ethanol and formaldehyde sensing characteristics of pseudo-peanut shaped iron oxide nano-particles are investigated. The iron oxide particles are synthesized through a facile cost effective wet chemical synthesis route. The X-ray diffraction pattern is used to confirm the hematite phase of the synthesized iron oxide particles. The electron microscopy studies reveal the pseudo-peanut like morphology of the particles. The sensing characteristics are measured by varying the operating temperature (300-375^{o}C) of the sensor and concentration of the organic vapors. In the studied operating temperature range, the sensing element shows maximum efficiency at ~350^{o}C where the estimated response towards 200 ppm ethanol and formaldehyde are found 78 % and 66 % respectively. The sensor can detect even 50 ppm of these vapors with promising response %. For sensing the vapors, the estimated values of response % and response time indicates that the sensor is more sensitive towards ethanol than formaldehyde. Poor selectivity of the sensor is revealed when selectivity coefficient values are

estimated considering total exposure time of vapors. On contrary, the estimated values of selectivity coefficients for limited time exposure are found comparatively higher which can be useful information for the development of selective ethanol sensor. For the detection of ethanol and formaldehyde vapors, the response of peanut shaped particles are further compared with the poly-disperse hematite particles. It is found that as compared to poly-disperse particles, peanut shaped particles are more sensitive towards the studied vapors.

Acknowledgement

The authors would like to express their gratitude to Director, CSIR-CMERI for his kind permission to publish the paper. The support provided by Council of Scientific and Industrial Research (CSIR), Govt. of India and the help rendered by the Scientific & Technical Staffs of Centre for Advanced Materials Processing (CAMP), CSIR-CMERI, Durgapur are sincerely acknowledged. The authors also wish to acknowledge Central Research Facility, CSIR-CMERI for providing the FESEM facility. Ms. P. Das thanks Department of Science and Technology, Govt. of India for supporting her research fellowship. Dr. K. Mukherjee wishes to acknowledge Department of Science and Technology, Govt. of India for providing him Inspire Faculty fellowship (Ref. DST/ IFA12-CH-43).

References

[1] Yang, S.; Xu, Y.; Sun, Y.; Zhang, G.; Gao, D. Size-Controlled Synthesis, Magnetic Property, and Photocatalytic Property of Uniform α-Fe_2O_3 Nanoparticles via a Facile Additive-Free Hydrothermal Route. *Cryst. Eng. Comm.* **2012**, 14, 7915-7921.

[2] Zhou, Y.X.; Yao, H.B.; Yao, W.T.; Zhu, Z.; Yu, S.H. Sacrificial Templating Synthesis of Hematite Nanochains from $[Fe_{18}S_{25}](TETAH)_{14}$ Nanoribbons: Their Magnetic, Electrochemical, and Photocatalytic Properties. *Chem. Eur. J.* **2012**, 18, 5073-5079.

[3] Tilley, S.D.; Cornuz, M.; Sivula, K.; Gratzel, M. Light-Induced Water Splitting with Hematite: Improved Nanostructure and Iridium Oxide Catalysis. *Angew. Chem. Int.* Ed. **2010**, 49, 6405-6408.

[4] Jin, W.; Dong, B.; Chen, W.; Zhao, C.; Mai, L.; Dai, Y. Synthesis and Gas Sensing Properties of Fe_2O_3 Nanoparticles Activated V_2O_5 Nanotubes. *Sens. Actuators B* **2010**, 145, 211-215.

[5] Chun, L.; Wu, X.; Lou, X.; Zhang, Y. Hematite Nanoflakes as Anode Electrode Materials for Rechargeable Lithium-Ion Batteries. *Electrochim. Acta* **2010**, 55, 3089-3092.

[6] Ma, J.; Teo, J. ; Mei, L. ; Zhong, Z. ; Li, Q.; Wang, T.; Duan, X.; Lian, J.; Zheng, W. Porous Platelike Hematite Mesocrystals: Synthesis, Catalytic and Gas Sensing Applications. *J. Mater. Chem.* **2012**, 22,11694-11700.

[7] Chen, J.; Xu, L.; Li, W.; Gou, X. α-Fe_2O_3 Nano-Tubes in Gas Sensor and Lithium Ion Battery Applications. *Adv. Mater.* **2005**,17, 582-586.

[8] Zhao, Y.M.; Li, Y.H.; Ma, R.Z.; Roe, M.J.; McCartney, D.G.; Zhu, Y.Q. Growth and Characterization of Iron Oxide Nanorods/ Nanobelts Prepared by a Simple Iron-Water Reaction. *Small* **2006**, 2, 422-427.

[9] Zhu, L.P.; Xiao, H.M.; Liu, X.M.; Fu, S.Y. Template-Free Synthesis and Characterization of Novel 3D Urchin-Like α-Fe_2O_3 Superstructures. *J. Mater. Chem.* **2006**, 16, 1794-1797.

[10] Pan, Y.; Gao, J.; Zhang, B.; Zhang, X.; Xu, B. Colloidosome-based Synthesis of a Multifunctional Nanostructure of Silver and Hollow Iron Oxide Nanoparticles. *Langmuir* **2010**, 26, 4184-4187.

[11] Lynch, J.; Zhuang, J.; Wang, T.; LaMontagne, D.; Wu, H.; Cao, Y.C. Gas-Bubble Effects on the Formation of Colloidal Iron Oxide Nanocrystals. *J. Am. Chem. Soc.* **2011**, 133, 12664-12674.

[12] Pascu, O.; Carenza, E.; Gich, M.; Estrade, S.; Peiro, F.; Herranz, G.; Roig, A. Surface Reactivity of Iron Oxide Nanoparticles by Microwave-Assisted Synthesis; Comparison with the Thermal Decomposition Route. *J. Phys. Chem. C* **2012**, 116, 15108-15116.

[13] Zhou, X.; Yang, H.; Wang, C.; Mao, X.; Wang, Y.; Yang, Y.; Liu, G. Visible Light Induced Photocatalytic Degradation of Rhodamine B on One Dimensional Iron Oxide Particles. *J. Phys. Chem. C* **2010**, 114, 17051-17061.

[14] Sharma, G.; Jeevanandam, P. Synthesis of Self-Assembled Prismatic Iron Oxide Nanoparticles by a Novel Thermal Decomposition Route. *RSC Adv.* **2013**, 3, 189-200.

[15] Lee, H.U.; Lee, S.C.; Lee, Y.C.; Vrtnik, S.; Kim, C.; Lee, S.G.; Lee, Y.B.; Nam, B.; Lee, J.W.; Park, S.Y.; Lee, S.M.; Lee, J. Sea-Urchin-Like Iron Oxide Nanostructures for Water Treatment. *J. Hazard. Mater.* **2013**, 262, 130-136**.**

[16] Yu, S.H.; Shin, J.; Kim, J.J.; Lee, K.J.; Sung, Y.E. Vertically Aligned Iron Oxide Nanotube Arrays and Porous Magnetite Nanostructures as Three-Dimensional Electrodes for Lithium Ion Microbatteries. *RSC Adv.* **2012**, 2, 12177-12181.

[17] Cui, H.; Liu, Y.; Ren, W. Structure Switch between α-Fe_2O_3, γ-Fe_2O_3 and Fe_3O_4 During the Large Scale and Low Temperature Sol-Gel Synthesis of Nearly Monodispersed Iron Oxide Nanoparticles. *Adv. Powder Technol.* **2013**, 24, 93-97.

[18] Guo, H.; Barnard, A.S. Naturally Occurring Iron Oxide Nanoparticles: Morphology, Surface Chemistry and Environmental Stability. *J. Mater. Chem. A* **2013**, 1, 27-42.

[19] Mohapatra, M.; Anand, S. Synthesis and Applications of Nano-Structured Iron Oxides/Hydroxides: A Review. *Int. J. Eng. Sci. Tech.* **2010**, 2,127-146.

[20] Zhu, M.; Wang, Y.; Meng, D.; Qin, X.; Diao, G. Hydrothermal Synthesis of Hematite Nanoparticles and Their Electrochemical Properties. *J. Phys. Chem. C* **2012**, 116, 16276-16285.

[21] Chen, H.; Sulejmanovic, D.; Moore, T.L.; Colvin, D.C.; Qi, B.; Mefford, O.T.; Gore, J.C.; Alexis, F.; Hwu, S.J.; Anker, J.N. Iron-Loaded Magnetic Nanocapsules for Ph-Triggered Drug Release and MRI Imaging. *Chem. Mater.* DOI: 10.1021/cm404168a.

[22] Zhu, J.; SimonNg, K.Y.; Deng, D. Hollow Cocoon-Like Hematite Mesoparticles of Nanoparticle Aggregates: Structural Evolution and Superior Performances in Lithium Ion Batteries. *ACS Appl. Mater. Interfaces* **2014**, 6, 2996-3001.

[23] Bolanz, R.M.; Wieczorek, M.W.; Caplovicova, M.; Uhlik, P.; Gottlicher, J.; Steininger, R.; Majzlan, J. Structural Incorporation Of As^{5+} into Hematite. *Environ. Sci. Technol.* **2013**, 47, 9140-9147.

[24] Khan, S.B.; Rahman, M.M.; Akhtar, K.; Asiri, A.M.; Seo, J.; Han, H.; Alamry, K. Novel and Sensitive Ethanol Chemi-Sensor based on Nanohybrid Materials. *Int. J. Electrochem. Sci.* **2012**, 7, 4030-4038.

[25] Flueckiger, J.; Ko, F.K.; Cheung, K.C. Micro Fabricated Formaldehyde Gas Sensors. *Sensors* **2009**, 9, 9196-9215.

[26] Sutka, A.; Mezinskis, G. Sol-Gel Auto-Combustion Synthesis of Spinel-Type Ferrite Nanomaterials. *Front. Mater. Sci.* **2012**, 6, 128-141.

[27] Guo, X.; Mao, D.; Lu, G.; Wang, S.; Wu, G. Glycine-Nitrate Combustion Synthesis of CuO-ZnO-ZrO_2 Catalysts for Methanol Synthesis from CO_2 Hydrogenation. *J. Catal.* **2010**, 271, 178-185.

[28] Patil, K.C.; Aruna, S.T.; Mimani, T. Combustion Synthesis: An Update. Curr. Opin. Solid State Mater. Sci. **2002**, 6, 507-512.

[29] Mimani, T.; Patil, K.C. Solution Combustion Synthesis of Nanoscale Oxides and their Composites. Mater. Phys. Mech. **2001**, 4, 134-137.

[30] Deshpande, K.; Mukasyan, A.; Varma, A. Direct Synthesis of Iron Oxide Nanopowders by the Combustion Approach: Reaction Mechanism and Properties. *Chem. Mater.* **2004**, 16, 4896-4904.

[31] Karmakar, M.; Mondal, B.; Pal, M.; Mukherjee, K. Acetone and Ethanol Sensing of Barium Hexaferrite Particles: A Case Study Considering the Possibilities of Non-Conventional Hexaferrite Sensor. *Sens. Actuators B* **2014**, 190, 627-633.

[32] Navale, S.C.; Ravi, V.; Mulla, I.S.; Gosavi, S.W.; Kulkarni, S.K. Low Temperature Synthesis and NO_x Sensing Properties of Nanostructured Al-Doped ZnO. *Sens. Actuators B* **2007**, 126, 382-386.

[33] Sharma, G.; Jeevanandam, P. Synthesis of Self-Assembled Prismatic Iron Oxide Nanoparticles by a Novel Thermal Decomposition Route. *RSC Adv.* **2013**, 3, 189-200.

[34] Jihua, W.; Xiutao, G.; Xingqin, L. Preparation of Spinel-Type $Cd_{1-x}Mg_xGa_2O_4$ Gas-Sensing Material by Sol-Gel Method. *Sens. Actuators B* **2006**, 115, 622-625.

[35] Zhang, L.; Zhao, J.; Lu, H.; Gong, L.; Li, L.; Zheng, J.; Li, H.; Zhu, Z. High Sensitive and Selective Formaldehyde Sensors based on Nanoparticle-Assembled ZnO Micro-Octahedrons Synthesized by Homogeneous Precipitation Method. *Sens. Actuators B* **2011**, 160, 364-370.

[36] Xu, J.; Jia, X.; Lou, X.; Xi, G.; Han, J.; Gao, Q. Selective Detection of HCHO Gas Using Mixed Oxides of $ZnO/ZnSnO_3$. *Sens. Actuators B* **2007**, 120, 694-699.

[37] Mukherjee, K.; Majumder, S.B. Reducing Gas Sensing Behavior of Nano-Crystalline Magnesium-Zinc Ferrite Powders. *Talanta* **2010**, 81, 1826-1832.

[38] Biswas, S.K.; Pramanik, P. Studies on the Gas Sensing Behaviour of Nanosized $CuNb_2O_6$ towards Ammonia, Hydrogen and Liquefied Petroleum Gas. *Sens. Actuators B* **2008**, 133, 449-455.

[39] Bhargav, K.K.; Maity, A.; Ram, S.; Majumder, S.B. Low Temperature Butane Sensing using Catalytic Nano-Crystalline Lanthanum Ferrite Sensing Element. *Sens. Actuators B* **2014**, 195, 303-312.

[40] Mukherjee, K.; Majumder, S.B. Analyses of Conductance Transients to Address the Selectivity Issue of Zinc Ferrite Gas Sensors. *Electrochem. Solid-State Lett.* **2010**, 13, J25- J27.

[41] Maity, A.; Mukherjee, K.; Majumder, S.B. Addressing the Cross-Sensitivity of Magnesium Zinc Ferrite Towards Reducing Gas Sensing Using Pattern Recognition Techniques. Sensor Lett., **2012**, 10, 916-920.

[42] Vaishampayan, M.V.; Deshmukh, R.G.; Mulla, I.S. Influence of Pd Doping on Morphology and LPG Response of SnO_2. *Sens. Actuators B*, **2008**, 131, 665-672.